

# Multiprocess Laser Lifting-Off for Nanostructured Semiconductive Hydrogels

Yufeng Tao,\* Chunsan Deng, Jing Long, JingWei Liu, Xuejiao Wang,\* Xiaoxian Song, Chengchangfeng Lu,\* Jingjing Yang, Hui Hao, Chengbo Wang, and Wenguang Zhang

Semiconductive hydrogels denote a strategically valuable platform associated with interdisciplinary fields by double advantages of metals and organisms (eco-friendliness, structural flexibility, mixed conduction, real-time responsiveness, scalable fabrication, and chemical stability). Nevertheless, the orthodox chemical/physical methods processing hydrogels yield planar-like layers or rough structures without ultrafine feature size or manipulative performance, falling short of  $\mu$ -robotics,  $\mu$ -electronics, or n-energy industries. Thereby, scaling the device's volume down and unleashing material's potential become crucially important for broadband applications. A femtosecond laser lifting-off technique is synthesized with self-assembly to break conventional volume/resolution limitation, enlarge the geometry-design capacity, and desirable electricity conduction for micro/nanosituations. Low-dimensional high-performance nanowires, electric circuits, ultrathin interdigital capacitors, manipulative photon filters, and metasurfaces are functionalized here. The repeated experiment concludes a high-density integration ability with a subminiature size down to  $10 \times 10 \times 0.02 \mu\text{m}^3$ , tunable electric conductivity up to  $1.17 \times 10^5 \text{ S m}^{-1}$ , and areal capacitance  $>16.2 \text{ mF cm}^{-2}$  for energy storage higher than those electrochemical double-layer ones. Large geometry capacity with nanometric resolution provides access to future-perspective optoelectronic products, n-energy, bioneural recordings, or interfaces of embedding conditions.

last decade.<sup>[1–8]</sup> SMH offered mixed conduction of electronic and ionic charge carriers,<sup>[4]</sup> desirable electric properties (charge carrier mobility  $>3 \text{ cm}^2 \text{ V}^{-1} \text{ s}^{-1}$ , work function  $>5 \text{ eV}$ , high Seebeck coefficient  $>10 \mu\text{V K}^{-1}$ ),<sup>[7]</sup> intriguing electroactive and mechanical properties<sup>[2,3b]</sup> for practical possibilities in wearable electronics, health monitoring or care systems.<sup>[4,5]</sup> Its intrinsic viscoelasticity and self-healing ability<sup>[9]</sup> alleviated the troublesome mismatch issues for man–machine interfaces or e-epidermis beyond those brittle metals. Versatile SMHs allowed chemical modification/grafting on its molecular chain,<sup>[1,3]</sup> acid/bases doping,<sup>[1c,d]</sup> thermal treatment,<sup>[6b]</sup> electrochemical gelation,<sup>[10]</sup> oxidative chemical vapor deposition, or worked as a carrier for doping nanofillers.<sup>[11,12]</sup> Besides, as was known, corrosive environment (acid,<sup>[1]</sup> alkali, or humidity), polar solvents,<sup>[6,9]</sup> and high temperature<sup>[7]</sup> were the least-inviting conditions for metal electronics, but they enhanced SMHs for better electric conduction, TE properties,<sup>[7]</sup> or self-healing<sup>[9]</sup> instead of performance degradation.

Myriad effective synthesis strategies or fabrications were invented to fully unleash SMHs potential via electrochemical gelation,<sup>[10]</sup> pen lithography,<sup>[12]</sup> or spray ejecting.<sup>[13,14]</sup> However, the fabricated SMH electronics still took the rough macroshape (resolution at a sub-millimeter level by the latest 3D printing technique<sup>[2]</sup>) or planar-like films<sup>[11]</sup> without customizable geometries at high freedom. Bulky SMH electronics lost ultrafine function programmability and were physically inaccessible to

## 1. Introduction

Hydrogel electronics (constructed on solution-processable semiconductive hydrogel with p-electron delocalization)<sup>[1]</sup> promised numerous biological applications,<sup>[2,3]</sup> e-skins,<sup>[4]</sup> sensors,<sup>[5]</sup> bioelectrodes,<sup>[6]</sup> thermoelectric (TE),<sup>[7]</sup> capacitors,<sup>[8]</sup> and spintronics. This champion material, semiconductive hydrogel (SMH),<sup>[3,6]</sup> radically rebuilt our conceptions of modern electronics in the


Y. Tao, X. Wang, X. Song  
Institute of Micro-nano Optoelectronics and Terahertz Technology  
Jiangsu University  
Zhenjiang 212013, China  
E-mail: taoyufeng@ujs.edu.cn; wsnwp520@sina.com

Y. Tao, C. Deng, J. Long, J. W. Liu, C. Wang, W. Zhang  
Wuhan National Laboratory for Optoelectronics  
Huazhong University of Science and Technology  
Wuhan 430074, China

C. Lu  
Whiting School of Engineering  
Johns Hopkins University  
Baltimore, MD 21218-2688, USA  
E-mail: c9lu@ucsd.edu

J. Yang  
Institute of Technological Sciences  
Wuhan University  
Wuhan 430072, China

H. Hao  
Jiangsu Key Laboratory of Optoelectronic Technology  
Nanjing Normal University  
Nanjing 210023, China

 The ORCID identification number(s) for the author(s) of this article can be found under <https://doi.org/10.1002/admi.202101250>.

DOI: 10.1002/admi.202101250

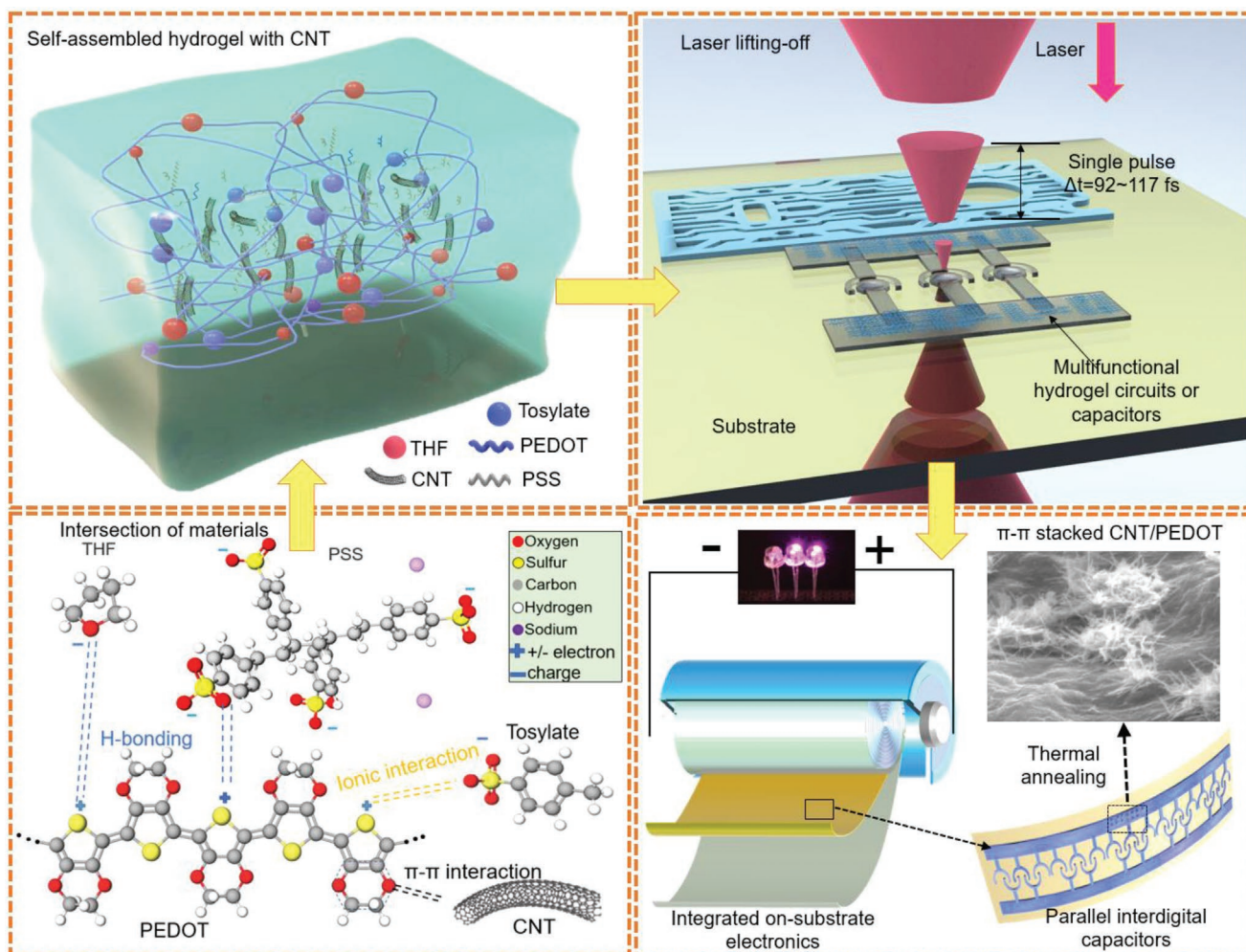


**Figure 1.** A schematic of the multiprocess fs-LLO nano/microengineering to scale down semiconductive hydrogels. Hydrogel precursor was balanced by self-assembly. Femtosecond laser pulse hit the spinning-coated precursor film on the substrate to lift off unwanted regions. After thermal annealing, the semicrystallized hydrogel presented a high-conductive nanostructure with  $\pi$ -stacked CNTs on SMH film, polymeric chains, and CNTs.

the embeddable applications.<sup>[11–14]</sup> However, the spatial resolution of central processing units (CPUs) was  $<22$  nm in integrated electronics, interspacing width  $<50$  nm, the current density of transistors approached  $10^6$  mm<sup>-2</sup>, and the number of electric components in logic circuits exceed  $10^4$  mm<sup>-2</sup>. The SMH applications<sup>[1–13]</sup> lagged far beyond Moore's law,<sup>[14b,c]</sup> falling short of the fast-developed n-electronics,<sup>[14c]</sup>  $\mu$ -mechanics, and n-photonics. Resultantly, it remained technologically challenging to integrate SMH at high density, which stifled its rapid innovations and broadband applications.

Unfortunately, SMH naturally lacked the vital moieties<sup>[15]</sup> that be readily crosslinked by ultraviolet lithography or two-photon polymerization.<sup>[16]</sup> Thus, SMH got perennially prohibited from optically transferring complex patterns onto chips. To break these geometry/resolution limitations and radically functionalize SMH, a facile multiprocess femtosecond laser lifting-off (fs-LLO, **Figure 1**; Figure S1, Supporting Information) incorporating with self-assembly was demonstrated to tailor SMHs geometries, dimensions, and properties. The multiprocess fs-LLO inherited advantages of material and the high

efficiency of laser processing, scaled device volume down, and boosted their optoelectronic performance by micro/nanogeometries. Then, measurement confirmed the high performance of nanostructured interdigital capacitors, electrical circuits, photon filters, and metasurfaces. All devices exhibited desirable utility concerning real-time responsiveness, energy conversion behaviors, surface properties, soft mechanics, and high spatial resolution that were formidable to 3D printing techniques.<sup>[12–14]</sup>

## 2. Results and Discussion

The blended poly(3,4-ethylenedioxythiophene) (PEDOT):poly(styrenesulfonate) (PSS)<sup>[1]</sup> stood out among conductive polymers due to its multitude merits of hydrogel nature (Table S1, Supporting Information),<sup>[3,6]</sup> low thermal conduction ( $<0.3$  W m<sup>-1</sup> K<sup>-1</sup>),<sup>[18]</sup> high power factor ( $10$ – $400$   $\mu$ W m<sup>-1</sup> K<sup>-2</sup>),<sup>[19]</sup> easy patterning, and optical clarity ( $>90\%$  at a thickness of  $<30$  nm). Herein, we blended PEDOT:PSS solution with small-molecule tetrahydrofuran (THF, boiling point  $\approx 65.4$  °C),

single-wall carbon nanotube (CNT),<sup>[11,16,17]</sup> and tosylate (0.05 wt%) based on miscibility. The hydroxyl-grafting CNTs (Young's modulus > 0.8 GPa,<sup>[19]</sup> area >1000 m<sup>2</sup> g<sup>-1</sup>, thermal conduction >3000 W m<sup>-1</sup> K<sup>-1</sup>) unveiled uniform dispersion due to  $\pi$ - $\pi$  interaction.<sup>[20,21]</sup> THF interconnected PSS molecules through hydrogen bonding.<sup>[15,22]</sup> Self-assembly generated a homogeneous precursor solution after balancing all interactive effects.

Physical/chemical properties of the in-solution PEDOT precursor varied a lot through our modification. Stiffness (Figure S2, Supporting Information) and Young's modulus (0.05–0.27 MPa) got noticeable improvement if heated or adding more CNTs (from 0.12–0.57 to 3.1–22.6 MPa when crystallized film with CNT). Thicker SMH nanocomposite precursor presented dark blue (Figure S3, Supporting Information), in other words, the optical clarity<sup>[1c,5a,6b]</sup> depended on the thickness from rotation speed (Figure S6, Supporting Information). Adding THF to 0.4 wt% shifted its UV absorption ratio in the 400 to 1000 nm range (Figure S4, Supporting Information). The rapid thermal annealing (135 °C) decreased the surface energy (water-contact angle altered from 52.7° to 108.2°, seen in Figure S5, Supporting Information).

The schematic procedure of the multiprocess fs-LLO contained three stepwise operations (Figure S1, Supporting Information). Step 1. In-solution self-assembly<sup>[20–22]</sup> turned the mixture into a homogeneous precursor by balancing intermolecular forces.<sup>[21]</sup> Tosylate (0.05 wt%) enabled the long chain of PEDOT molecules to congregate by physical crosslinks to stabilize holes through local charge neutralization.<sup>[23]</sup> Step 2. Spin-coating prepared the ultrathin SMH film on substrates (Figure S6, Supporting Information) at controllable thickness. Pulsed laser beam got MHz acoustic-optical modulation as an invisible dicing knife<sup>[24,25]</sup> to hit spin-coated film at the pre-designed trajectories. Step 3. Heating or thermal annealing dedoped the residual volatile THF, insulative PSS, and water off for more crystalline PEDOT-rich domains.<sup>[1b,6b]</sup>

Fs-LLO overcame thermal interaction issues<sup>[26–28]</sup> as a non-contact ultrafast transfer route (Equations (S1)–(S5), Supporting Information) with huge design space,<sup>[25]</sup> and broke the curb of generic 3D printing<sup>[2,29]</sup> for delicate micro/nanostructures. Multifunctional SMH geometries were prototype designed and rapidly fabricated on ultrathin SMH film. The as-fabricated SMH nanowires (Figures S7a and S8, Supporting Information) exhibited ultrafine dimensions (linewidth < 50 nm, roughness < 5 nm, thickness < 20 nm) even at a high laser-scanning speed of 2 mm s<sup>-1</sup>. The entire fabrication required no sacrificial layers, tedious transferring platforms, vacuum chambers, masks, or molds of conventional imprinting technologies. Moreover, thermal annealing formed PEDOT-rich domain with hybrid hydrogel/crystal/CNT construction (investigated by XRD test showing a more crystalline process<sup>[18c–f]</sup> in Figure S10, Supporting Information). CNTs interacted with the conjugated polymers in PEDOT rich phases (Figures 2a and 3b) to provide a mixed electron/hole transporting path.<sup>[23,30]</sup>

## 2.1. Semiconductive SMH Nanowires

Sub-micrometer voxel (laser focus radius < 0.3  $\mu$ m through a large-N.A. oiled 100 $\times$  objective lens) of fs-LLO guaranteed

a nanometric edge roughness (Videos S1 and S2, Supporting Information) in fabricating straight or curvy 1D nanowires (Figure 2b; Figure S7a, Supporting Information). The large surface-to-volume ratio increased the surficial interface contact with ethanol/glycol, which separated PEDOT from PSS for more compact nanochannels. Nanowires were customized here and micrographed by three methods: an atomic force microscope (Dimension Edge, Bruker Nano Surfaces, Figures S7 and S8, Supporting Information), a digital laser confocal microscope (LCM, Keyence VHX-7000, lateral resolution < 4 nm, longitudinal resolution < 1 nm, Figure 2b), and a field-emission scanning electron microscope (SEM) with energy-dispersive X-ray spectroscopy (Edx, Figure S12, Supporting Information), the measured linewidth reached 47.2, 48.3, and 44.7 nm (Table S2, Supporting Information), respectively, promising a practical integration density of >2  $\times$  10<sup>5</sup> cm<sup>-2</sup> processing SMH materials with enough interspace to avoid short circuit from occurring.

A visual Raman mapping technique (resolution of each pixel, in extracting 1441 cm<sup>-1</sup> peak characteristic of PEDOT C=C backbone) reflected out the material distribution on a footprint area of 5  $\times$  5  $\mu$ m<sup>2</sup>. PEDOT was highlighted as brilliant blue (Figure 2b, Supporting Information) by inelastic scattering of photons in straight lines, black blank indicated the lifted-off area without residue. In spectra (Figure S13, Supporting Information), the precursor spectrum portrayed all characteristic peaks of used hydrogel. After thermal annealing, PEDOT feature blue-shifted, magnified, and overwhelmed CNT, THF, and PSS, implying PEDOT eventually dominated the electric properties of SMH, and concentration of THF and PSS was significantly reduced by thermal annealing.

The virtuosity of modeling tools (AutoCAD, UG, or Solidworks) allowed fs-LLO to transfer complex layouts to substrates taking only a few minutes much faster than 3D extrusion or lithography of taking hours for simple patterns. Ubiquitous curvilinear electric circuits (Figure 2c; Figure S7b, Supporting Information), meandering patterns, and even specific microscale letters (“electrically semiconductive hydrogel” in Video S3 of the Supporting Information, “PEDOT:PSS” in Figure 2d; Figure S14 and Video S4, Supporting Information) were single-step fabricated and identified. The flexibility of multiprocess fs-LLO offered more geometry-based functions outperforming those simple planar layers or films for nanostructured semiconductive devices. Beneficially, no apparent circuit-opening, overlapping, cracking, breakage or collapse occurs in these structures even after three-turn thermal annealing (constant 135 °C) for 20 min each turn.

To investigate electric performance, we first tested Seebeck coefficient<sup>[31]</sup> of SMH film from 20 to 150 °C (by NETZSCH, SBA-458), increasing from 8.81 to 15.3  $\mu$ V K<sup>-1</sup> at top at low-concentration of THF without CNTs, and declined to 14.32  $\mu$ V K<sup>-1</sup> at 145 °C (Figure S15, Supporting Information). Increasing concentration of THF and CNTs here predicted a higher Seebeck coefficient and better TE function (Seebeck coefficient  $\approx$  29.3  $\mu$ V K<sup>-1</sup>). However, the self-assembling effect and aggregated CNTs devastated the nanometric fabrication by the dopant-induced morphology modulation (Figure S11, Supporting Information).<sup>[7b–f,34]</sup> To satisfy the volume/resolution requirement for broad micro/nanoapplications, we abandoned the heavy-doping strategy for TE properties (Seebeck coefficient exceeding 200  $\mu$ V K<sup>-1</sup>),<sup>[7,15,18]</sup> which modulated molecular



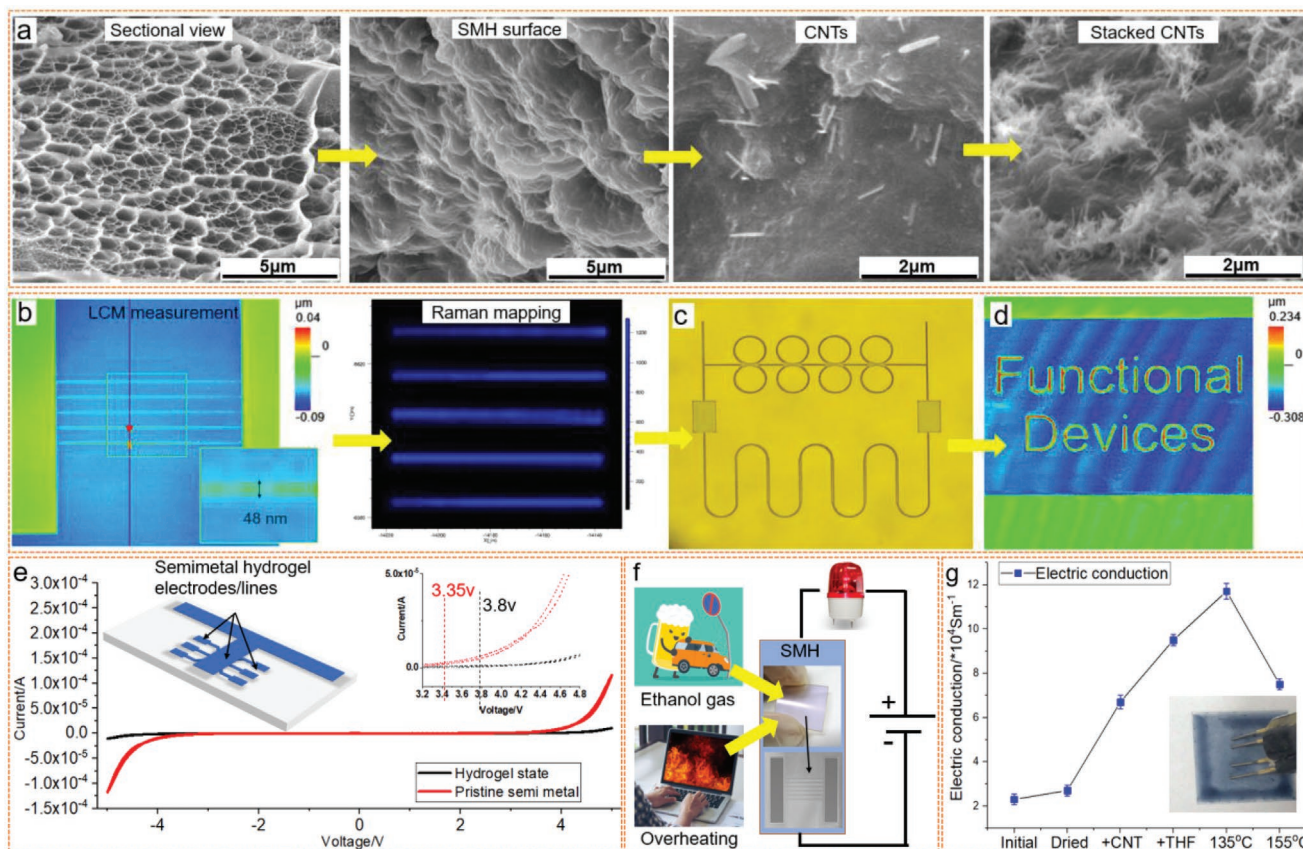


**Figure 2.** a) Local morphology of sectional view of inside hydrogel network → the dried crumpled hydrogel surface → the zoomed-in view of CNTs exposed on hydrogel surface → the semicrystallized stacked PEDOT nanorods in clusters. b) Laser confocal microscope images of SMH nanowires and Raman mapping. c) Curvilinear semiconductive circuits with bending angles exceeding 180 °C. d) 3D image of “functional devices” with a maximum thickness up to 234 nm. e) Repeated current–voltage scanning to determine open voltage threshold of SMH nanowires. f) Schematic illustration of on-chip nanowires used as sensor to alcohol or temperature. g) The electric conductivities of SMHs (tuned by adding CNT or THF, or annealed at different temperatures), peaking at around 134 °C  $\approx 1.17 \times 10^5 \text{ S m}^{-1}$ .

morphology to damage nanometric geometric features (Figure S9, Supporting Information).

Subsequently, a Keithley semiconductive parameter analyzer (Agilent, B-1500) figured out a current threshold voltage at 4.1 and 3.4 V for hydrogel and crystalline states, the weak current skyrocketed at a sharp slope if an applied voltage exceeding a threshold (Figure 2e) or adding alcohols. The tunable electric conduction by dropping acid/bases, ionic liquid or heating could be recorded from peripheral circuits as an environment sensor (Figure 2f). The electric conductivity of SMH film shifted to  $1.17 \times 10^5 \text{ S m}^{-1}$  by the four-probe resistance test (Figure 2g), which was substantially improved from our previous work ( $< 5 \times 10^3 \text{ S m}^{-1}$ )<sup>[16]</sup> fluctuated between styrenesulfonic acid-doping method ( $4.22 \times 10^4 \text{ S m}^{-1}$ )<sup>[18d]</sup> and ionic treatment ( $1.439 \times 10^5 \text{ S m}^{-1}$ )<sup>[7d]</sup> and still lower than fully crystallized PEDOT ( $3 \times 10^6 \text{ S m}^{-1}$ )<sup>[18a]</sup>

135 °C annealing provided the optimal condition for balancing self-assembly, semicrystallization (containing both long-chain molecules and some crystalline PEDOT), and no brittle mechanics or fractures, therefore, the highest electric conduction was obtained. As root cause, CNTs ( $> 10^6 \text{ S m}^{-1}$ ) tangled with PEDOT-rich domains to constitute more electron-transport pathways under constant volume (Figure 2a; Figure S10,

Supporting Information). Carbon atoms of  $\text{SP}^2$  ring connected PEDOT holes (positive charges), contributing to an electron/hole conductivity higher than polyaniline, pyrrole (Table S1, Supporting Information), thiophene, acetylene (Table S1, Supporting Information), or II–VI metal sulfide/oxide.

## 2.2. Electrode-Changeable Interdigital Capacitors

Energy storage or conversion promised a paradigmatic solution for the globally increasing energy crisis.<sup>[32]</sup> Thereby, the micro/nanoscale capacitors applicable for next-generation e-skins,<sup>[4]</sup> electricity generators,<sup>[34]</sup> and bioelectronics<sup>[2]</sup> became an imperative demand. Scientists and engineers kept looking for a combination of dimension reduction and large scale energy storage volume for years.<sup>[32–34]</sup> Unfortunately, the intensively studied 3D-printed electronics<sup>[2,13,14,29]</sup> still stayed at macroscope with millimeter-scale resolution out of the implantable occasions. The effective micro/nanoengineering of capacitors remained rare but highly valued.

The topology controllability of the fs-LLO incorporating with SMH offered a new solution to the energy crisis by ultrathin hydrogel-based energy storage devices.<sup>[35]</sup> Here, we fabricated

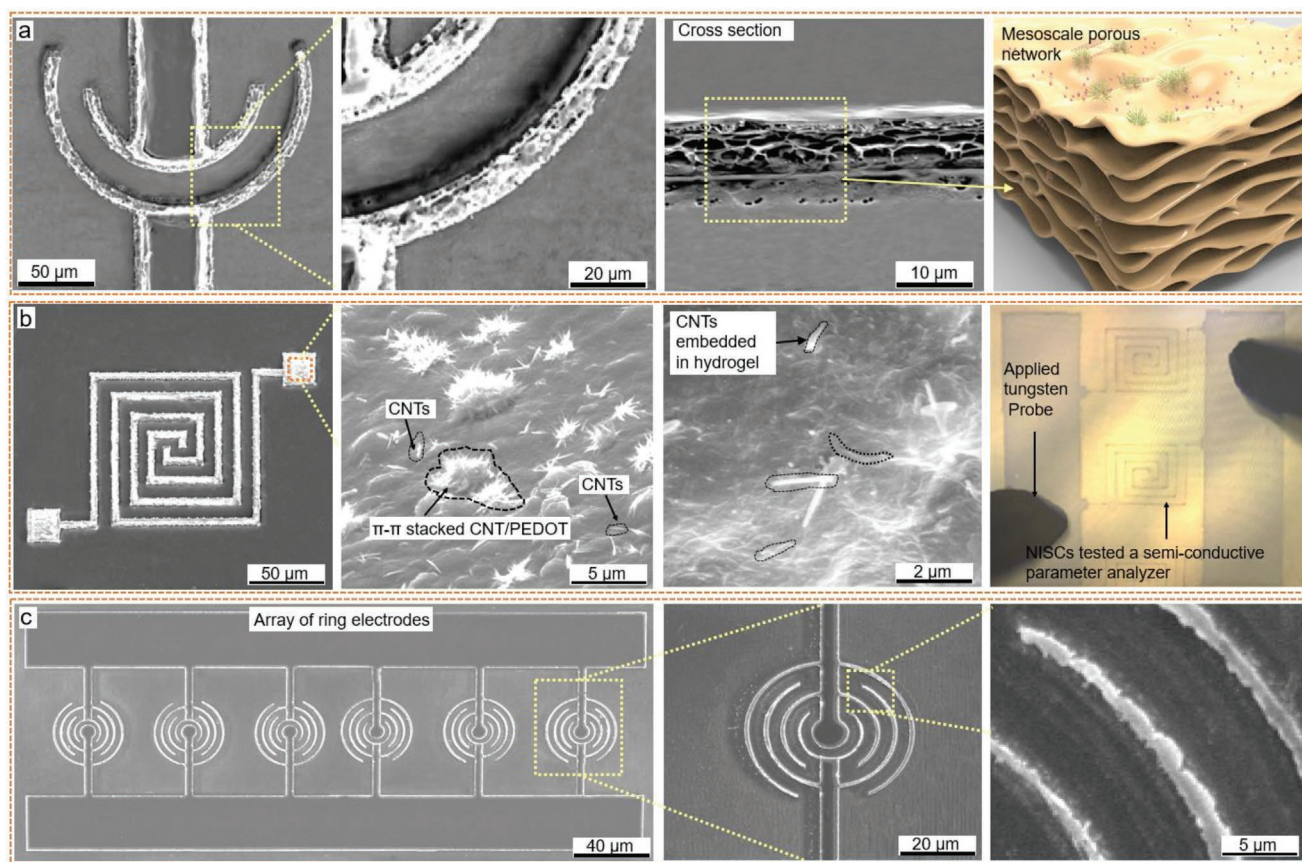


**Figure 3.** a) SEM images of a ring-shaped interdigital capacitor at an approximate thickness of 4 μm, zoomed-in, and cross-view of the porous matrix, which contributed a better diffusion path for ionic solution or electrolyte. b) SEM images of a square-shaped interdigital capacitor after rapid thermal annealing and a camera view of the integrated capacitors under test. c) SEM images of a ring-shaped interdigital capacitor and zoomed-in view of the ring electrodes.

nanometric single-layer interdigital capacitors (NSICs). The minimum volume scaled down to  $30 \times 30 \times 0.02 \mu\text{m}^3$  (Figure 3) at a subminiature ratio of three-order magnitude than conventional electrochemical electrodes. The freestanding NSICs promised a diversity of shape-changed electrodes (Figure 3a) at tunable interspacing and thickness (down to 19.2 nm controlled by spin-coating speed). Moreover, the mixed electron/hole transportation also provided another method to manipulate capacitance done by adjusting the material ratio. The NSICs of intrinsic hydrogel nature also offered opportunities for bioapplications due to the soft mechanics.

As was known,<sup>[33–35]</sup> the stored charge originated from the fast surface redox reactions of PEDOT, NSICs held higher pseudo capacitance density than electrochemical ones constrained at the limited smooth surface. Porous morphologies of the hydrogel network (Figures 2a and 3a) provided abundant channels and huge volume for electrolyte diffusion to facilitate energy-store responsiveness. The high dielectric constant electrolyte (ethanol glycol in Figure 4) flowed throughout SMH structures and interacted with the aggregated PEDOT molecules for better material use.

Thermal annealing evaporated the volatile insulating THF, PSS, and moisture off (Raman spectra in Figure S13, Supporting Information) for a highly concentrated semimetal morphology.

PEDOT molecular chain folded and noncovalently aggregated by  $\pi$ - $\pi$  stacking effect,<sup>[21]</sup> changing the initial Fermi glass to a semicrystal with a shorter distance for transporting electrons or holes.<sup>[15–18]</sup> The PEDOT aggregated into the PEDOT-rich domains (Figures 2a and 3b) attractive to CNTs. Some other PSS/THF molecules formed a PSS/THF-rich domain on the material interface (Figures 3b) without  $\pi$ - $\pi$  stacking interaction with CNTs. Long-chain PEDOT molecules, CNTs, and crystalline intertwined a compact space, the  $\pi$ -conjugation chains with p-electrons entangled with carbon atoms providing more electric nanochannels.

Volume reduction and shaping ability of fs-LLO extend the capability of NSICs to on-chip integrate with peripheral circuits or nanogenerators<sup>[35,36]</sup> to harvest energy, or to protect vulnerable electrical chips from volt overloading, or to supply power. Manipulative electrode geometries (the square-shaped and ring-shaped electrodes with tunable interspacing in Figure 3b,c, and Videos S1 and S2, Supporting Information) became real (Figure 4a,b) due to the flexible laser parameters (Table S2, Supporting Information).<sup>[27,28]</sup> The evidence showed that NSICs featured desirable cycling stability with capacitance retention of up to 82% over 2 K cycles applied  $-5$  to  $5/0$  to  $5$  V alternative voltage covering DC to radiofrequency formidable to current low-efficiency lithium batteries or carbon electrodes. In



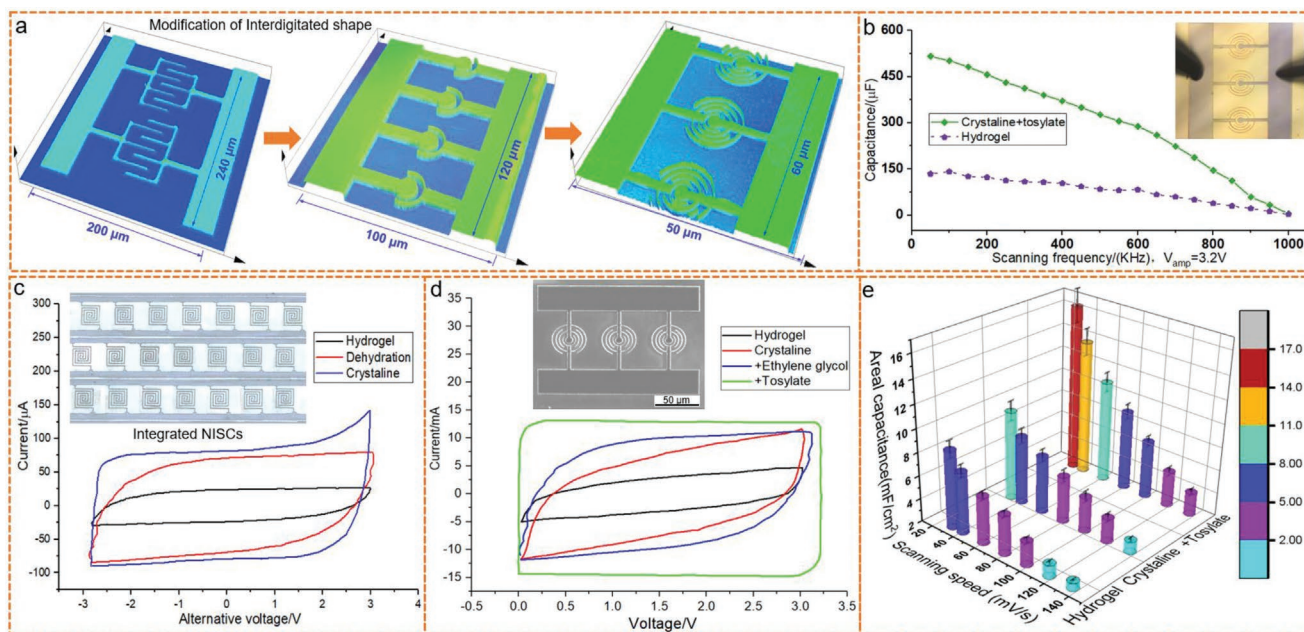


**Figure 4.** a) LCM images of the electrode-altered NSICs, dimensions  $< 240 \times 240 \times 10 \mu\text{m}^3$ . b) The pseudocapacitance of ring-electrode NSICs declined at incremental scanning frequency (from 10 KHz to 1 MHz). Capacitance downscaled to less than  $10 \mu\text{F}$  at 10 MHz from initial  $480 \mu\text{F}$ , conveying a better energy storage behavior at low frequency ( $< 200 \text{KHz}$ ). c) I/V response curves of square-electrode NSICs at normal, dehydrated at  $30^\circ\text{C}$ , and thermal crystallized, respectively. d) I/V response of ring-electrode NSICs. Curves presented a quasi-rectangle hysteresis curve by applying ethylene glycol as electrolytes. e) Summary of tested areal capacitance correlated with the scanning speeds and postprocessed states.

repeated electric tests, capacitance-to-frequency manifested a declining trend (from  $> 140 \mu\text{F}$  at 10 KHz  $\rightarrow 102 \mu\text{F}$  at 200 KHz  $\rightarrow 65 \mu\text{F}$  at 500 KHz  $\rightarrow 15 \mu\text{F}$  at 800 KHz  $\rightarrow 5 \mu\text{F}$  at 1 MHz  $\rightarrow < 10 \text{pF}$  at 10 MHz, Figure 4b), but still higher than reported transition metal oxides.<sup>[37]</sup> Effect of electrode shape gave a deviation of areal capacitance and responsive curve (Figure 4c,d), ring-shaped electrode demonstrated a standard rectangle hysteresis curve (Figure 4d).

If NSICs immersed in the anion,<sup>[15,23]</sup> tosylate, the ionic intersection created more holes leading to polarons formation (“neutral” PEDOT or  $\text{PEDOT}^{+1} \rightarrow \text{PEDOT}^{+2}$ ).<sup>[30]</sup> If immersed in a glycol environment, the dipole–dipole interaction between glycol and thiophene rings of PEDOT<sup>[22]</sup> stretched out the molecular chain for better phonon or electron transport, leading to large energy storage (Figure 4c,d). Therefore, glycol or tosylate solution recombined the NSICs as recommended electrolytes. The repeated tests found that the low-frequency scanning voltage provided a desirable areal capacitance of NISC up to  $16.2 \text{mF cm}^{-2}$  (Figure 4e, footprint area calculated from the digital dimension of Figure 4a). NSICs were totally metal-free, easy to integrate, capacity/geometry-tunable, and highly tolerant of sweating human skin, humidity, or ion<sup>[7,9]</sup> well-suited to wearable electronics.

### 2.3. On-Chip Photonic Applications

As was known, programmable on-chip photonic structures offered huge interest to optical sensors,<sup>[38]</sup> light-manipulation (Figure 5),<sup>[39]</sup> information-encoding,<sup>[40a]</sup> data storage, or anticounterfeiting, which usually depended on metals or

their oxides (Au, Ag,  $\text{TiO}_2$ , etc.). Here, we employed fs-LLO to manipulate SMH nanowire array as photonic crystal (PC, Figure 5a–c) to select photons for structural coloration (purple, brilliant blue, grass green, yellow, orange, red, and dark red, Figure 5a). The nanometric feature (Figure 5b) and dimensional flexibility promised a serial of optical wavelengths<sup>[40b]</sup> covering visible and invisible ranges. Interestingly, the PCs maintained desirable electrical conductivity when using as a photonic device.<sup>[39]</sup>

The three-letter pattern (U.J.S., seen in Figure 5c) consisted of geometry-shifted PCs that enabled highlighted structural coloration for displaying<sup>[40]</sup> or information storage. Proper design of PC geometries promised more complex patterns and better controllability on PCs. To study the photon filtering utility, we detected the transmission spectra by exploiting an optical spectrograph (Princeton, SCT-320) through each PC sequentially at the resolution of 0.2 nm (Figure 5d). The retrieved spectral peaks unanimously matched with observed coloration.

Antireflection coating or signal selector played as critical components to reduce glare and light reflection loss regarding modern optic or optoelectronic systems for better optical clarity in camera lens, display screen, glasses lens, and the glass cover of photovoltaic solar cells.<sup>[41–45]</sup> Manufacturers of LCD, cathode-ray tubes, and aerospace sensor products often added antireflection coating<sup>[41]</sup> to optical parts for prolonging service life. However, traditional methods sacrificed shape controlling ability such as spin-coating, vacuum evaporation, etc.<sup>[42]</sup> In literature, the impedance matching layers of metal coating,<sup>[43]</sup> vanadium dioxide films,<sup>[44,45]</sup> or using graphene<sup>[46]</sup> was reliable only in a narrow band ( $< 0.8 \text{THz}$ ). Worse, the 2D materials generally lacked the self-supporting ability for complex structures.

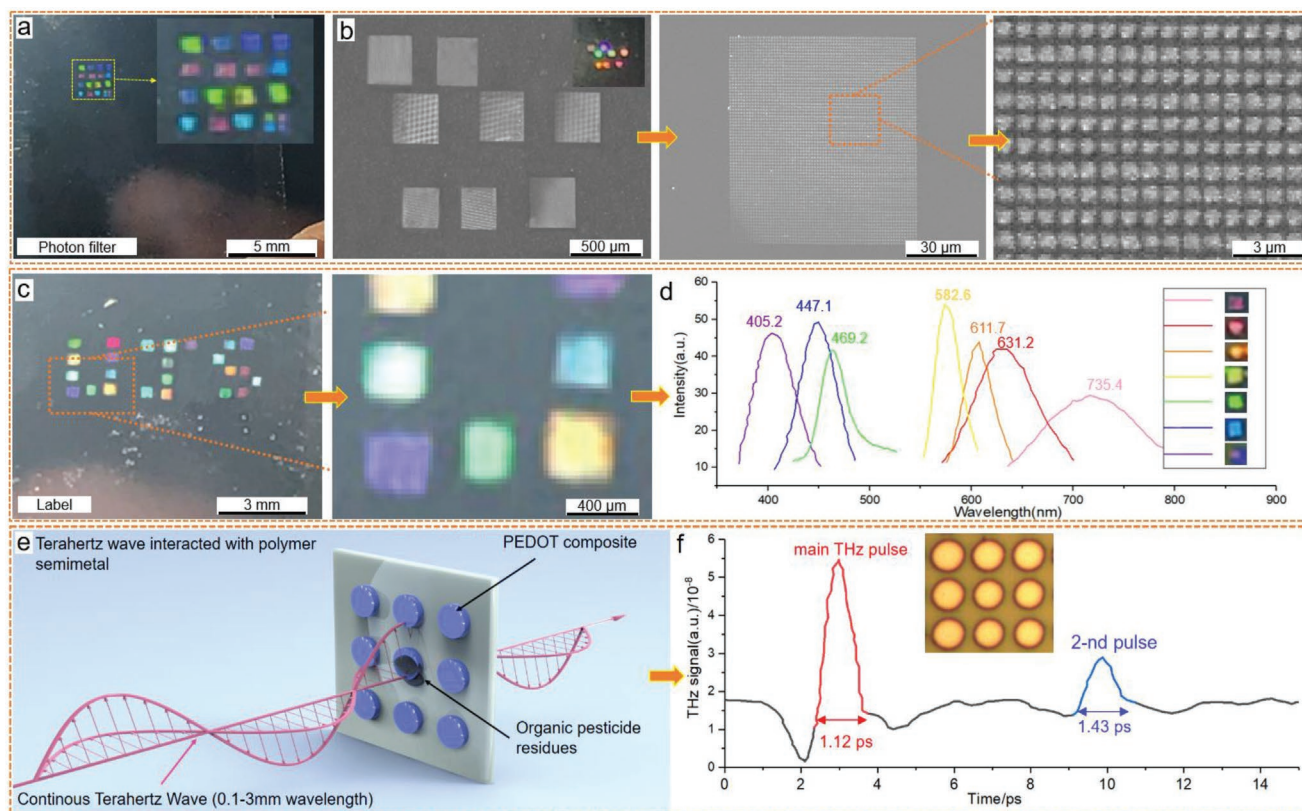


**Figure 5.** a) Camera view of an on-chip  $4 \times 4$  PC array using SMH material. b) SEM images of on-chip PCs, and magnified single PC for details. c) PCs arranged for epitomizing three letters “U.J.S.” d) Transmittance spectra of each PC on a single chip. e) Schematic illustration of THz spectra measurement with the as-prepared SMH metasurface. f) THz time-domain Transmission spectra of SMH film containing double pulses due to reflection effect.

To extend the SMH application to THz band, we transferred the microstructured SMH cylinder array onto a glass substrate as THz metasurface hypothesizing with local resonance effect.<sup>[42]</sup> It was investigated using a commercial terahertz time-domain spectroscopy. The as-fabricated THz metasurface was projected by a  $0.5 \text{ mm}^2$  focused THz wave from spectrometer with Apodization windowing (wavelength ranging from 0.01 to 1 mm, Advantest, TAS7500, Figure 5e) to reflect the transmission spectrum (covering 0.2 to 1.2 THz at stepsize of 1.9 GHz). Interestingly, the transmission band expanded to over 1 THz (Figure 5f) wider than previously reported matching layers,<sup>[41–46]</sup> which also suppressed secondary reflection at the interface.

We picked two commonly used chlorinated pesticides, Imidacloprid (a biotoxic pesticide) and Triadimefon (a fungicide of moderate toxicity, Figure S16, Supporting Information), incorporating our prepared THz metasurface for THz time-domain spectral detection. The THz spectra depicted that  $\mu$ -structures of cylinders (radius  $\approx 45 \text{ }\mu\text{m}$ , thickness  $\approx 4 \text{ }\mu\text{m}$ ) array improved the intensities by triple times (Figure S17, Supporting Information), implying that SMH metasurface effectively suppressed secondary reflection at the interface. Spectral curves illustrated more distinctive rotational and vibrational characters. Undeniably, THz time-domain spectrometer could analyze toxic substances<sup>[46]</sup> at a better signal quality with the assistance of SMH metasurface.

### 3. Conclusion

Self-assembly succeeded in electric conduction improvement of PEDOT:PSS hydrogel without sacrificing the spin-coated surface roughness (thickness controlled down to 20 nm). The small molecular-weight polar THF and CNTs concentrated long-chain PEDOT molecules for a shorter electron/hole transporting path by noncovalent effect. Mechanics of the modified PEDOT film varied in stiffness (from  $<4000$  to  $>12\,000 \text{ }\mu\text{N}$ ) by self-assembly and postprocessing (Rapid thermal annealing at  $135 \text{ }^\circ\text{C}$ ), and its Seebeck coefficient got improvement (as high as  $15.3 \text{ }\mu\text{V K}^{-1}$ ) with electric conduction (up to  $1.17 \times 10^5 \text{ S m}^{-1}$ ). The multi-process fs-LLO technique combined self-assembly, and thermal annealing succeeded in breaking the resolution/dimension/properties limitations of 3D-printed hydrogels by inducing the unprecedented spatial resolution (linewidth  $< 50 \text{ nm}$ , at least two-order better than the extrusion 3D printing) and maintaining a vast shape/pattern design capacity, promising the hydrogel electronics readily integrated with electronic or even photonic products.

Broadband application of semiconductive hydrogels was technologically guaranteed by the rapid optical transferring micro/nanodesign. Following that, we demonstrated nanowire array (density  $> 10^4 \text{ mm}^{-1}$ ), electrical circuits at nearly arbitrary layouts (bending angle  $> 180^\circ$ ), ultrathin supercapacitors (areal capacitance  $> 16.2 \text{ mF cm}^{-2}$  and allowed for massive



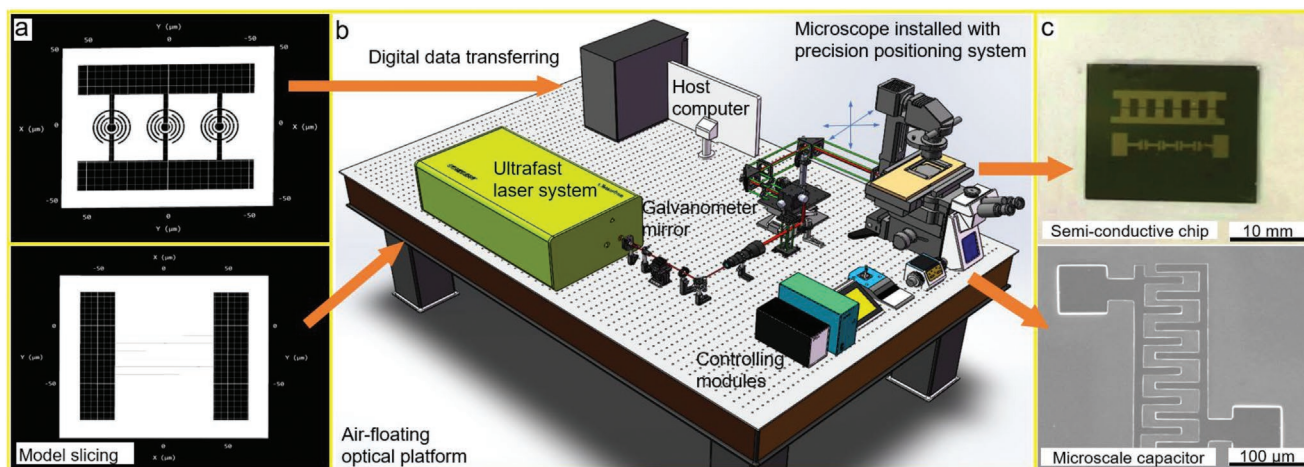


**Figure 6.** Schematic illustration of the streamlined multiprocess fs-LLO. a) Logically inverted 3D models designed by CAD software (a ring-shaped capacitor and a nanowire array). b) The established computer-aided ultrafast laser system. c) Typical SMH products of the retrieved macro electrodes and a microscale capacitor.

integration), manipulative photon filters (wavelength covered the visible spectrum), and THz metasurface (transmission band exceeded 1 GHz) for the first time as a guideline. The multiprocess fs-LLO implied the next-generation hydrogel electronics by the in-depth programming of hydrogel components or systems to the future-perspective  $\mu$ -electronics, n-photonics, biosensors, n-energy devices of interdisciplinary fields.

#### 4. Experimental Section

**Preparation of PEDOT–THF–CNT Nanocomposite:** All used reagents were at high purity 99.9+%, and commercially available from Sigma-Aldrich. PEDOT:PSS solution (1.4 wt%) was diluted by deionized water to 0.7 wt%, and was stirred with 0.2 wt% tetrahydrofuran, 0.2 wt% hydroxyl-modified carbon nanotube, and 0.05 wt% tosylate. After one-day sealed placement for self-assembly, spin-coating transformed the precursor into film with even surface roughness (<2 nm at the thickness of 20–30 nm, rotation speed at 1000 rpm for 90 s) before ultrafast fs-LLO process.

**Mask-Free fs-LLO Process:** Fs-LLO operated at the laboratory (humidity < 55%, temperature  $\approx$ 20 °C), rapid thermal annealing was implemented in a vacuum environment with <  $10^{-3}$  Pa air pressure. The fs-laser system (Figure 6) for massively reproducible n/ $\mu$ -optoelectronics based on a mode-locked solid Ti:Sapphire laser (Chameleon Discovery, Coherent), emitting a wavelength-tunable pulsed laser beam (100 fs pulse width, wavelength covered visible, and invisible ranges from 650 to 1200 nm). The terminal microscope (OLYMPUS IX 73) was equipped with a charge-coupled device (CCD), dichroic mirror, and an objective-selective system. The oil-immersed objective lens (40 $\times$ , 60 $\times$ , 100 $\times$ , N.A. = 1.4) focused the laser beam at the liquid-to-substrate interface. A 2D galvanometric scanning mirror (intelliSCAN III 140, SCANLAB) was implanted to cowork with a 3D movable platform. The entire optical system was fixed on an air-floating platform to isolate vibrational interferences.

**Rapid Thermal Annealing:** Thermal annealing of SMH devices was implemented in a low-vacuum (air pressure <  $10^{-3}$  Pa) tubular furnace (GSL-1100X, Heifei Kejing) with a temperature resolution of 1 °C and range from 20 to 150 °C at the speed of 10 °C min $^{-1}$ . Each period lasted 20 min for the three circles of entire annealing.

**Electrical Performance Characterization:** Electric performance was measured using a semiconductive devices analyzer, including a high-resolution digital source meter (B1500A, Keysight) and a manual operation platform (MPS150, Cascade Microtech) to determine the

I/V characters. A pair of water-proof tungsten probes touched the SMH devices for inputting voltage and collecting transient current (pA resolution). Four-probe square impedance tester (KQY-1, Jingge electronics, 0.01  $\Omega$  resolution) gave the sheet resistance ( $R_s$ ) of SMH material. Electrical conductivity  $\sigma$  was calculated using the equation  $\sigma = 1/(R_s \times d)$ , where  $d$  denotes the thickness of films.

**Nanoscale Characterization:** Nanoscale characterization of nano/micro-engineered PSM devices was replied on a field-emission electron microscope (FEI Nova NanoSEM 450) at acceleration voltages of 2–10 kV, magnifying 100–30 000 times, or an ESEM (Thermo Scientific Quanta 200, FEI) on low-vacuum condition for SEM images or secondary-electron images. All specimen were freezing-to-drying processed before SEM for more details. Energy-dispersive X-ray spectroscopy (Edx) was carried with SEM characterization. A laser confocal microscope (LEXT OLS5000, Olympus) was utilized to nondestructively evaluate surface profile and thickness. Microscope Olympus-X71 recorded the CCD images.

**Thermogravimetric Analysis:** Thermogravimetric analysis was implemented in a thermally controlled chamber and monitored by a thermogravimetric analyzer (Pyris-1, Perkinelmer). The ambient temperature was up to 600 °C, and weight resolution was small down to 0.1  $\mu$ g. Temperature ramped up at 10 °C min from 20 to 600 °C to dehydrate hydrogel and record weight loss.

**Raman Spectrum Analysis:** Raman spectroscopy was obtained through a Raman spectrometer at laser wavelength of 532 nm (InVia, Renishaw), ranging from 200 to 2000 nm using 60 $\times$  objective lens (N.A. = 0.75). Laser power irradiating on NECHs was 5 mW. Data interrogation of Raman spectra was at time intervals of 3 s each.

**Seebeck Coefficient Test:** SMH film and commercial PEDOT:PSS film were postprocessed at the thickness of about 1  $\mu$ m on a 10  $\times$  10 mm $^2$  substrate, then substrates were put into the tester chamber (SBA 458 Nemesis, NETZSCH), where temperature range varied between 20 and 150 °C for simultaneously detecting Seebeck coefficient and resistance.

**Mechanics Test:** Mechanical properties of SMH film were reflected using a micromechanics instrument (FT-MTA02, FemtoTools). The micromechanics platform (compressive and tensile test) operated on the principle of nanoindentation. A micrometer-robotic system combines the FT-FS1000 mechanical force sensor (tip radius of probes is 0.5  $\mu$ m) with the FT-UMS1002 (optical microscope system) for tensile, compressive, and adhesive forces tests.

**XRD and UV–Vis Test:** XRD test analyzed phase transfer (from hydrogel state to a semicrystallized nanostructure) for structural characterization. A Bruker D8 Discover diffractometer was carried out with an X-ray source operating at 30 kV, 30 mA. Data of dried SMH



hydrogel and the semicrystallized SMH were collected, respectively. UV absorption spectra in the range of 400–1000 nm were obtained using a UV–vis spectrometer (UV2450, Simadzu).

## Supporting Information

Supporting Information is available from the Wiley Online Library or from the author.

## Acknowledgements

This research was financially supported by the National Key R&D Program of China (2017YFB1104300, SQ2018YFB110138), National Natural Science Foundation of China (61774067), National Science Foundation (CMMI 1265122), National Natural Science Youth Fund of China (61805094), China Postdoctoral Science Foundation (2017M622417), and the Fundamental Research Funds for the Central Universities (HUST:2018KFYXKJC027). All authors sincerely thank Prof. Xiong Wei, and Dr. Fan Xuhao of Huazhong University of Science and Technology for experimental instruction.

## Conflict of Interest

The authors declare no conflict of interest.

## Data Availability Statement

The data that supports the findings of this study are available in the supplementary material of this article.

## Keywords

femtosecond laser lifting off, function-integrated manufacturing, nanoenergy,  $\pi$ - $\pi$  stacking

Received: July 19, 2021

Revised: September 14, 2021

Published online: November 23, 2021

- [1] a) B. Y. Lu, H. W. Yuk, S. T. Lin, N. N. Jian, K. Qu, J. K. Xu, X. H. Zhao, X. H. Pure, *Nat. Commun.* **2019**, *10*, 1043; b) T. Someya, Z. Bao, G. G. Malliaras, *Nature* **2016**, *540*, 379; c) J. Ouyang, *Displays* **2013**, *34*, 423; d) G. H. Kim, L. Shao, K. Zhang, K. P. Pipe, *Nat. Mater.* **2013**, *12*, 719.
- [2] H. Yuk, B. Y. Lu, S. Lin, K. Qu, J. K. Xu, J. H. Luo, X. H. Zhao, *Nat. Commun.* **2020**, *11*, 1604.
- [3] a) H. L. Sun, H. A. Klok, Z. Y. Zhong, *Biomacromolecules* **2018**, *19*, 1697; b) M. Elmahmoudy, S. Inal, A. Charrier, Ilke Uguz, G. Malliaras, S. Sanaur, *Macromol. Mater. Eng.* **2017**, *302*, 1600497; c) S. Zhang, Y. Chen, H. Liu, Z. Wang, H. Ling, C. Wang, J. Ni, B. Çelebi-Saltik, X. Wang, X. Meng, H.-J. Kim, A. Baidya, S. Ahadian, N. Ashammakhi, M. R. Dokmeci, J. Trivas-Sejdic, A. Khademhosseini, *Adv. Mater.* **2020**, *32*, 1904752; d) X. Fan, W. Nie, H. Tsai, N. Wang, H. Huang, Y. Cheng, R. Wen, L. Ma, F. Yan, Y. Xia, *Adv. Sci.* **2019**, *6*, 1900813; e) U. Lang, N. Naujoks, J. Dual, *Synth. Met.* **2009**, *159*, 473.
- [4] a) T. Q. Trung, N. E. Lee, *Adv. Mater.* **2016**, *28*, 4338; b) L. W. Lo, J. Zhao, H. Wan, Y. Wang, S. Chakraborty, C. Wang, *ACS Appl. Mater. Interfaces* **2021**, *13*, 21693.
- [5] a) E. Roh, B. Hwang, D. Kim, B. Kim, N. Lee, *ACS Nano* **2015**, *9*, 6252; b) Y. Liang, A. Offenhäusser, S. Ingebrandt, D. Mayer, *Adv. Healthcare Mater.* **2021**, *10*, 2100061.
- [6] a) H. W. Yuk, B. Y. Lu, X. H. Zhao, *Chem. Soc. Rev.* **2019**, *48*, 1642; b) Y. Wang, C. X. Zhu, R. Pfattner, H. P. Yan, Z. N. Bao, *Sci. Adv.* **2017**, *3*, 1602076; c) O. Dimitriev, D. A. Grinko, Yuriy Noskov, N. Ogurtsov, A. Pud, *Synth. Met.* **2009**, *159*, 2237.
- [7] a) Y. Wang, L. Yang, X. Shi, L. Chen, M. Dargusch, J. Zou, Z. Chen, *Adv. Mater.* **2019**, *31*, 1807916; b) X. Guan, W. Feng, X. Wang, R. Venkatesh, J. Ouyang, *ACS Appl. Mater. Interfaces* **2020**, *12*, 13013; c) T. A. Yemata, Y. Zheng, A. Kyaw, X. Z. Wang, J. Song, W. Chin, J. W. Xu, *RSC Adv.* **2020**, *10*, 1786; d) J. Atoyok, M. Burton, J. McGettrick, M. J. Carnie, *Polymers* **2020**, *12*, 559; e) T. A. Yemata, Y. Zheng, A. Kyaw, X. Wang, J. Song, W. Chin, J. W. Xu, *Org. Electron.* **2020**, *81*, 105682; f) D. Yun, J. Jung, K. Kim, H. Ra, J. Kim, B. S. Choi, J. Jang, M. Seol, Y. Jeong, *Appl. Surf. Sci.* **2021**, *533*, 149584.
- [8] H. S. Kim, J. Lee, S. K. Lee, Y. Chun, C. Park, J. Jin, H. U. Lee, S. Kim, *J. Cleaner Prod.* **2021**, *284*, 125449.
- [9] a) Y. Li, X. Li, S. M. Zhang, L. Liu, L. N. Hamad, S. Bobbara, D. Pasini, F. Cicoira, *Adv. Funct. Mater.* **2020**, *30*, 2002853; b) Y. Li, S. Zhang, N. Hamad, Kyoungoh Kim, L. Liu, Michael Lerond, F. Cicoira, *Macromol. Biosci.* **2020**, *20*, 2000146; c) S. Zhang, F. Cicoira, *Adv. Mater.* **2017**, *29*, 40.
- [10] V. Feig, H. Tran, M. Lee, K. Liu, Z. Huang, L. Beker, D. Mackanic, Z. Bao, *Adv. Mater.* **2019**, *31*, 1902869.
- [11] N. Chen, B. W. Luo, Anoop C. Patil, J. H. Wang, G. G. L. Gammad, Z. G. Yi, X. G. Liu, S. Yen, S. Ramakrishna, N. Thakor, *ACS Nano* **2020**, *14*, 8059.
- [12] H. U. Lee, J. H. Jin, S. W. Kim, *J. Ind. Eng. Chem.* **2019**, *71*, 184.
- [13] D. N. Heo, S. J. Lee, R. J. Timsina, X. Y. Qiu, N. J. Castro, L. G. Zhang, *Mater. Sci. Eng., C* **2019**, *99*, 582.
- [14] a) K. Tian, J. Y. Bae, S. E. Bakarich, C. H. Yang, R. D. Gately, G. M. Spinks, M. Panhuis, Z. G. Suo, J. J. Vlassak, *Adv. Mater.* **2017**, *29*, 1604827; b) R. Chen, *Int. J. Extreme Manuf.* **2020**, *2*, 022002; c) M. Waldrop, *Nature* **2016**, *530*, 144.
- [15] a) O. Bubnova, Z. U. Khan, H. Wang, S. Braun, D. R. Evans, M. Fabretto, P. Hojati-Talemi, D. Dagnelund, J. B. Arlin, Y. H. Geerts, *Nat. Mater.* **2014**, *13*, 190; b) S. Khodakarimi, M. H. Hekhmatoar, M. Nasiri, M. Khaleghi Moghaddam, F. Abbasi, *J. Mater. Sci.: Mater. Electron.* **2016**, *27*, 1278.
- [16] Y. F. Tao, C. Y. R. Wei, J. W. Liu, C. S. Deng, S. Cai, W. Xiong, *Nanoscale* **2019**, *11*, 9176.
- [17] C. Y. Wang, K. L. Xia, H. M. Wang, X. P. Liang, Z. Yin, Y. Y. Zhang, *Adv. Mater.* **2018**, *31*, 1801072.
- [18] a) S. Rudd, J. F. Franco-Gonzalez, S. K. Singh, Z. U. Khan, X. Crispin, J. Andreasen, I. Zozoulenko, D. Evans, *J. Polym. Sci. Pol. Phys.* **2017**, *56*, 97; b) W. L. Ding, X. L. Peng, Z. Z. Sun, K. Bi, Y. Q. Zhang, Y. L. Wang, L. Ji, H. Y. He, *Mater. Adv.* **2021**, *2*, 2009; c) Z. A. King, C. M. Shaw, S. A. Spanning, D. C. Martin, *Polymers* **2011**, *52*, 1302; d) J. Kim, C. Park, S. Im, H. Lee, J. H. Kim, *RSC Adv.* **2019**, *9*, 4028; e) Y. L. Kang, S. Ibrahim, S. Pichiah, *Bioresour. Technol.* **2015**, *189*, 364; f) V. Sabatini, V. Pifferi, S. Checchia, S. Rebecani, H. Farina, M. Aldo Ortenzi, L. Falciola, *Polymers* **2018**, *10*, 770.
- [19] T. Park, T. C. Park, B. Kim, H. Shin, E. Kim, *Energy Environ. Sci.* **2013**, *6*, 788.
- [20] a) J. H. Deng, J. Luo, Y. L. Mao, S. Lai, Y. N. Gong, D. C. Zhong, T. B. Lu, *Sci. Adv.* **2020**, *10*, 9976; b) S. Grimme, *Angew. Chem., Int. Ed.* **2008**, *47*, 3430.
- [21] D. P. Malenov, G. V. Janjic, V. B. Medakovic, M. B. Hall, S. D. Zaric, *Coord. Chem. Rev.* **2017**, *345*, 318.
- [22] V. Mihali, A. Honciuc, *ACS Nano* **2019**, *13*, 3483.

- [23] a) A. De Izarra, S. Park, J. Lee, Y. Lansac, Y. H. Jang, *J. Am. Chem. Soc.* **2018**, *140*, 5375; b) M. Y. Teo, N. Kim, S. Kee, B. S. Kim, G. Kim, S. Hong, S. Jung, K. Lee, *ACS Appl. Mater. Interfaces* **2017**, *9*, 819; c) Q. Tai, B. Chen, F. Guo, S. Xu, X. Z. Zhao, *ACS Nano* **2011**, *5*, 3795; d) W. Jeong, G. Gwon, J. Ha, D. Kim, K.-J. Eom, J. H. Park, S. J. Kang, B. Kwak, J.-I. Hong, S. Lee, D. C. Hyun, S. Lee, *Biosens. Bioelectron.* **2021**, *171*, 112717.
- [24] M. Malinauskas, *Light: Sci. Appl.* **2016**, *5*, 16133.
- [25] a) N. Yulianto, A. Refine, A. Syring, N. Majid, S. Mariana, P. Schnell, R. A. Wahyuono, K. Triyana, F. Meierhofer, W. Daum, F. Abdi, T. Voss, H. Wasisto, A. Waag, *Microsyst. Nanoeng.* **2021**, *7*, 32; b) S. J. Kim, H. E. Lee, H. Choi, Y. Kim, J. H. We, J. S. Shin, K. J. Lee, B. J. Cho, *ACS Nano* **2016**, *10*, 10851; c) C. Zhu, D. Guo, D. Ye, S. Jiang, Y. Huang, *ACS Appl. Mater. Interfaces* **2020**, *12*, 37354.
- [26] a) A. Rahaman, A. Kar, X. Yu, *Opt. Express* **2019**, *27*, 5764; b) R. Weber, T. Graf, C. Freitag, A. Feuer, T. Kononenko, V. I. Konov, *Opt. Express* **2017**, *25*, 3966; c) F. Masoud, S. M. Sapuan, M. K. A. Mohd Ariffin, Y. Nukman, E. Bayraktar, *Polymers* **2020**, *12*, 1332.
- [27] R. Stoian, J. Colombier, *Nanophotonics* **2020**, *9*, 4665.
- [28] M. Hase, P. Fons, K. Mitrofanov, A. V. Kolobov, J. Tominaga, *Nat. Commun.* **2015**, *6*, 8367.
- [29] S. Lee, M. Wajahat, J. H. Kim, J. Pyo, W. S. Chang, S. H. Cho, J. T. Kim, S. K. Seol, *ACS Appl. Mater. Interfaces* **2019**, *11*, 7123.
- [30] a) J. Rivnay, S. Inal, B. A. Collins, M. Sessolo, E. Stavrinidou, X. Strakosas, C. Tassone, D. M. DeLongchamp, G. G. Malliaras, *Nat. Commun.* **2016**, *7*, 11287; b) R. Del Olmo, N. Casado, J. L. Olmedo-Martínez, X. Wang, M. Forsyth, *Polymers* **2020**, *12*, 1981; c) M. Berggren, X. Crispin, S. Fabiano, M. P. Jonsson, D. T. Simon, E. Stavrinidou, K. Tybrandt, I. Zozoulenko, *Adv. Mater.* **2019**, *31*, 1805813.
- [31] a) D. Kim, Y. Kim, K. Choi, J. Grunlan, C. Yu, *ACS Nano* **2020**, *4*, 513; b) Z. Fan, H. Cheng, X. Guan, C. Wang, K. Sun, J. Ouyang, *Macromol. Rapid Commun.* **2018**, *39*, 1700727; c) Q. Wei, M. Mukaida, K. Kirihaara, Y. Naitoh, T. Ishida, *Materials* **2015**, *8*, 732.
- [32] A. S. Aricò, P. Bruce, B. Scrosati, J. M. Tarascon, W. Schalkwijk, *Nat. Mater.* **2005**, *4*, 366.
- [33] X. Q. Zhang, X. B. Cheng, Q. Zhang, *J. Energy Chem.* **2016**, *25*, 967.
- [34] Q. Jiang, C. S. Wu, Z. J. Wang, A. C. Wang, J. He, Z. L. Wang, H. N. Alshareef, *Nano Energy* **2018**, *45*, 266.
- [35] X. Liu, Z. Xu, A. Iqbal, M. Chen, N. Ali, C. T. J. Low, R. R. Qi, J. T. Zai, X. F. Qian, *Nano-Micro Lett.* **2021**, *13*, 54.
- [36] D. Yoo, J. Kim, J. H. Kim, *Nano Res.* **2014**, *7*, 717.
- [37] a) J. Meyer, S. Hamwi, M. Kröger, W. Kowalsky, T. Riedl, A. Kahn, *Adv. Mater.* **2012**, *24*, 5408; b) E. Singh, P. Singh, K. S. Kim, G. Y. Yeom, H. S. Nalwa, *ACS Appl. Mater. Interfaces* **2019**, *11*, 11061; c) J. Shi, J. Zhang, L. Yang, M. Qu, D. C. Qi, K. H. L. Zhang, *Adv. Mater.* **2021**, 2006230, <http://doi.org/10.1002/adma.202006230>.
- [38] Y. Huang, L. X. Liu, X. Yang, X. Y. Zhang, B. Yan, L. Wu, P. J. Feng, X. D. Lou, F. Xia, Y. L. Song, F. Y. Li, *Small* **2021**, *17*, 2006723.
- [39] K. Wang, R. Dahan, M. Shentcic, Y. Kauffmann, A. B. Hayun, O. Reinhardt, S. Tsesses, I. Kaminer, *Nature* **2020**, *582*, 50.
- [40] a) Y. Qi, Y. W. B. Niu, S. F. Zhang, S. L. Wu, L. Chu, W. Ma, B. T. Tang, *Adv. Funct. Mater.* **2019**, *29*, 1906799; b) I. B. Burgess, L. Mishchenko, B. D. Hatton, M. Kolle, M. Lončar, J. Aizenberg, *J. Am. Chem. Soc.* **2011**, *133*, 12430.
- [41] M. Mittendorff, S. Winnerl, T. Murphy, *Adv. Opt. Mater.* **2021**, *9*, 2001500.
- [42] W. Xu, L. J. Xie, J. F. Zhu, L. H. Tang, R. Singh, C. Wang, Y. Ma, H. Chen, Y. Ying, *Carbon* **2019**, *141*, 247.
- [43] a) T. Hasebe, S. Kawabe, H. Matsui, H. Tabata, *J. Appl. Phys.* **2012**, *112*, 094702; b) C. Wang, X. Li, Y. Huang, W. Xu, R. Zhou, R. Wang, L. Xie, Y. Ying, *Opt. Express* **2018**, *26*, 24992.
- [44] K. Zhang, Y. X. Fan, L. L. Xu, T. Liu, H. Liu, Z. Y. Tao, *Phys. Scr.* **2021**, *96*, 065503.
- [45] a) S. H. Lee, J. Choe, C. Kim, S. Bae, J. Kim, Q. Han Park, M. Seo, *Sens. Actuators, B* **2020**, *310*, 127841; b) S. Adak, L. N. Tripathi, *Analyst* **2019**, *144*, 6172.
- [46] a) C. Wang, Y. X. Huang, R. Y. Zhou, L. J. Xie, Y. Ying, *Opt. Express* **2020**, *28*, 12001; b) J. Qin, L. Xie, Y. Ying, *Food Chem.* **2017**, *224*, 262. c) L. Hou, W. Shi, C. Dong, L. Yang, Y. Wang, H. Wang, Y. Hang, F. Xue, *Spectrochim. Acta, Part A* **2021**, *246*, 119044.